MIT Open Access Articles

A Comparison of Airborne In Situ Cloud Microphysical Measurement with Ground-Based C-Band Radar Observations in Deep Stratiform Regions of African Squall Lines

A Comparison of Airborne In Situ Cloud Microphysical Measurement with Ground-Based C-Band Radar Observations in Deep Stratiform Regions of African Squall Lines

E. Drigeard,* E. Fontaine,* W. Wobrock,* A. Schwarzenböck,* C. Duroure,* E. R. Williams,[+]
B. Russell,[+,++] A. Protat,[#] J. Delanoë,[@] F. Cazenave,[&] and M. Gosset**

*Laboratoire de Météorologie Physique, Université Clermont Auvergne, Université Blaise Pascal, and CNRS, INSU, UMR 6016, Aubière, France
[+]Parsons Laboratory, Massachusetts Institute of Technology, Cambridge, Massachusetts
[#]Center for Australian and Weather Climate Research, Melbourne, Australia
[@]Laboratoire Atmosphère, Milieux, Observations Spatiales, Velizy, France
[&]Laboratoire d'étude des Transferts en Hydrologie et Environnement–Université Grenoble 1/IRD/CNRS, Grenoble, France
**IRD/LTHE–CNRM/GMME/MOANA, Toulouse, France

ABSTRACT

This study addresses clouds with significant ice water content (IWC) in the stratiform regions downwind of the convective cores of African squall lines in the framework of the French–Indian satellite *Megha-Tropiques* project, observed in August 2010 next to Niamey (13.5°N, 2°E) in the southwestern part of Niger. The objectives included comparing the IWC–Z reflectivity relationship for precipitation radars in deep stratiform anvils, collocating reflectivity observed from ground radar with the calculated reflectivity from in situ microphysics for all aircraft locations inside the radar range, and interpreting the role of large ice crystals in the reflectivity of centimeter radars through analysis of their microphysical characteristics as ice crystals larger than 5 mm frequently occurred. It was found that, in the range of 20–30 dBZ, IWC and C-band reflectivity are not really correlated. Cloud regions with high IWC caused by important crystal number concentrations can lead to the same reflectivity factor as cloud regions with low IWC formed by a few millimeter-sized ice crystals.

1. Introduction

For a better understanding and interpretation of radar measurements, numerous airborne research projects have compared radar signals with in situ microphysics measurements of clouds and precipitation (e.g., Brandes et al. 1995; Matrosov et al. 2002; Lawson and Zudema 2009; Zong et al. 2013). To achieve reliable results, such comparisons must overcome two major difficulties. The first one is the spatial and temporal collocation of aircraft position and radar pulse volume, and the second

one involves the retrieval of condensed water content and radar reflectivity factor from the measured in situ hydrometeor number distributions. This second step is further complicated when ice crystals occur, because their complex irregular crystal shape must also be taken into account when calculating the radar reflectivity factor Z (hereinafter often simply called *reflectivity*).

An appropriate method to collocate aircraft and radar beam is coordinated aircraft–radar strategies wherein the aircraft follows a fixed azimuthal orientation for which the radar performs a vertical or "range–height indicator" (RHI) scan (Hogan et al. 2003, 2006; Field et al. 2004; Plank et al. 1980). Then, radar pulse volume and aircraft position deviate by less than 1.5 km, although temporal differences of several minutes can occur. To correct for this deviation, the observed aircraft data have to be shifted spatially—for example, by using the measured wind component along the radar azimuth at the altitude of sample.

Plummer et al. (2010) used RHI and horizontal "plan position indicator" (PPI) scans to collocate radar pulse volume and aircraft during the Mesoscale Alpine Programme (MAP) in 1999, without a previous coordination strategy between radar and aircraft. Similar to Hogan et al. (2006), aircraft wind measurements were used to correct the time shift between radar pulse volume and aircraft location. Forward and backward trajectories of air parcels departing from the aircraft location were calculated for a time span of 5 min to identify the radar pixels responsible for the observed in situ microphysics. This method also allowed for collocating aircraft and radar with a high precision below 1 km.

In contrast to the above-mentioned studies, which all used surface precipitation radars, Heymsfield et al. (2005, hereinafter HEYM05) collocated airborne cloud observations with a stratospheric aircraft that was equipped with vertically downward–pointing radars of centimeter and millimeter wavelengths. Despite the important distance between tropospheric and stratospheric platforms, high spatial coincidence of better than 1 km and very good temporal coincidence was obtained between radar pulse volume and in situ microphysics.

Quantitative studies that compared observed reflectivity for centimeter wavelengths with the reflectivity calculated from in situ microphysics were undertaken by HEYM05 and Hogan et al. (2006, hereinafter HOG06). Both studies investigated ice clouds with ice water contents (IWC) that were typically below $0.3 \, \mathrm{g \, m^{-3}}$ and reflectivities that were between −20 and 20 dBZ. In both studies, IWC and reflectivity were calculated from the particle size distribution (PSD) of the cloud hydrometeors using the mass–diameter relationship $m = \alpha D^{\beta}$. In HEYM05, α and β were determined from in situ IWC measurements provided by a counterflow virtual impactor. HOG06 used for α and β the coefficients given by Brown and Francis (1995).

The clouds investigated in HEYM05 were convectively generated stratiform ice-cloud layers over Florida that were located in the upper troposphere in a temperature range from −25° to −50°C; those of HOG06 were midlatitude ice clouds over England that were encountered at altitudes from 4 to 8 km, with temperatures between −9° and −32°C. Both studies demonstrated that the IWC can be retrieved from radar observations at centimeter as well as millimeter wavelengths. Only a low number of observations with IWC > $0.5 \, \mathrm{g \, m^{-3}}$ and reflectivities > 15 dBZ were included in this study. For dense ice clouds with reflectivity larger than 10 dBZ, HEYM05 found distinct differences in the power-law relationship between IWC and radar reflectivity relative to clouds with low and medium IWC and reflectivity. Both datasets (those of HEYM05 and HOG06) were reanalyzed by Hogan et al. (2012), taking into account crystal habit in the form of aligned oblate spheroids, which allowed them to improve their previous results.

The particular subject of this study is the comparison of C-band ground-based reflectivity observations with in situ PSD measurements in dense ice clouds with values of 15 and 35 dBZ and with much higher IWC, ranging from 0.1 to $4 \, \mathrm{g \, m^{-3}}$. The clouds, which were investigated at altitudes from 5200 to 10 500 m, belonged to the stratiform outflow of deep convective systems over western Africa. Data were collected during the French–Indian satellite *Megha-Tropiques* project in August of 2010 (MT2010) next to Niamey (13.5°N, 2°E) in the southwestern part of Niger. Two precipitation radars were operated next to Niamey: the Massachusetts Institute of Technology (MIT) C-band radar (Russell et al. 2010) and the X-band radar of the Laboratoire d'étude des Transfers en Hydrologie et Environnement/ L'Institut de recherche pour le développement (LTHE/ IRD; Gosset et al. 2010).

The main focus of this study is to investigate the relationship between IWC and reflectivity of centimeter radars in deep stratiform anvils where significant IWC and large ice crystals prevail. This analysis uses the results of Fontaine et al. (2014), who retrieved IWC from the PSD measurements in a synergy with airborne cloud radar observations (Protat et al. 2004, 2007).

In the above-cited studies, the comparisons between radar and in situ observations were restricted to a limited number of observational points during periods of less than 10 min. In this study, we compare all aircraft in situ observations as long as the aircraft stays inside the range scanned by the ground radar. The case studies presented in this paper analyze flight observations for periods from 30–40 min up to 2.5 h. The fixed volumetric scanning protocol of weather radars allows the detection of any spatial point (or "voxel") once during a 10-min period. This leads to temporal deviations between radar beam and aircraft, which will be discussed in detail below.

In section 2 we present the observational techniques that were available for this airborne campaign (section 2a) and show how reflectivity was calculated from the in situ instrumentation (section 2b). Section 3 gives details about the meteorological radars and describes the technique developed to collocate aircraft and radar observations. Section 4 shows results for different observational days and discusses the differences between the retrieved in situ reflectivity and the collocated reflectivity observed by the ground radar. Section 5

TABLE 1. Flow chart of retrieval of IWC using a synergy of observations from in situ probes and airborne reflectivity measurement at 94 GHz (Fontaine et al. 2014).

1) Measurements of the reflectivity factor by the cloud radar RASTA provide $Z_{OBS}^{94\,GHz}$ above and below the aircraft.

2) In situ measurements of microphysics by cloud imagers 2D-S and PIP provide D_{max} (max dimension of the hydrometeors), $N(D_{max})$ (no. distribution of hydrometeors above and below the aircraft), and $A_s(D_{max})$ (aspect ratio of particle images).

3) Calculate reflectivity factor $Z_{calc}^{94\,GHz}$: $Z_{calc}^{94\,GHz} = \int N(D_{max})\sigma_{back}^{94\,GHz} dD_{max}$, where $\sigma_{back}^{94\,GHz} = \sigma_{back}^{94\,GHz}(D_{max}, n, \overline{A_s})$ = backscatter coefficient (**T** matrix), with $\overline{A_s} = \int A_s(D_{max}) dD_{max}$ = mean aspect ratio, n = refractive index = $n(n_{ice}, n_{air}, x_{ice})$ according to Maxwell Garnett (1904), $x_{ice} = m_{crys}/(\rho_{ice}V_{crys})$ = mass fraction of ice in a crystals, $m_{crys} = \alpha D_{max}^{\beta}$, and $V_{crys} = (\pi/6)D_{max}^3 A_s$.

4) Fitting $Z_{calc}^{94\,GHz} = Z_{OBS}^{94\,GHz}$ by variation of α and β provides $m = \alpha D_{max}^{\beta}$.

investigates the relationship between ice water mass and Rayleigh reflectivity for a range from 15 to 35 dBZ and the uncertainties occurring in the IWC estimate when the reflectivity factor of precipitation radars is used. Section 6 summarizes and discusses the findings.

2. Aircraft observations

a. Microphysical in situ probes

The French research aircraft Falcon 20 was equipped with a new generation of optical array probes [Stratton Park Engineering Company, Inc., 2D-Stereo (2D-S) and Droplet Measurement Technologies, Inc., (DMT) precipitation imaging probe (PIP)], which allow resolution of droplet and ice crystal size spectra in the size range from $10\,\mu m$ to 6.4 mm. All datasets from the microphysical probes were recorded and analyzed with a time resolution of 1 s and were averaged over a time period of 5 s. A description of the analysis technique used for these instruments during MT2010 is given in Fontaine et al. (2014). The analysis furnishes the maximum dimension of the hydrometeors D_{max} of the individual particles and the number distribution of the different particle sizes $N(D_{max})$.

The maximum dimension D_{max} as used in Fontaine et al. (2014) is defined as the longest straight line that covers the particle image and crosses at the same time the barycenter of the particle image. The extension of the particle image perpendicular to the D_{max} axis and crossing the barycenter is called the minor axis H. The resulting axis ratio H/D_{max} will be identified with the aspect ratio A_s of the particle.

Shattering artifacts were removed using interarrival time analysis between two ice particles. Interarrival time between two particles is defined as the time elapsed from the end of the first particle and the beginning of a second ice particle (Field et al. 2006; Korolev and Isaac 2005; Field et al. 2003; Korolev and Field 2015). The time threshold is calculated every second to take into account the inhomogeneity of cloud. Particles with an interarrival time that is than the time threshold are

rejected for the calculation of the ice particle concentration $N(D_{max})$. Moreover, truncated images of hydrometeors and sample volume are corrected using the "center in" method given by Heymsfield and Parrish (1978).

Microphysical observations were performed at flight levels between 3500 and 10 500 m. The melting level prevailed for all flights at 4.7 km. Thus, microphysical measurements were done in regions of strong warm precipitation, in the melting layer, in mixed-phase regions, and in pure ice clouds with IWC up to 4 g m^{-3}. We focus in this study on entirely glaciated regions in stratiform tropical clouds wherein no more liquid droplets were detected.

b. Calculation of the radar reflectivity from in situ microphysics

The calculation of the radar reflectivity factor is based on the knowledge of the size distributions for number, shape, and mass of the hydrometeors encountered during MT2010. Particle number concentration and shape are given by the optical probes, but the mass of the hydrometeors has been retrieved using a synergy between in situ observations with microphysical probes and reflectivity measured with the French Radar Aéroporté et Sol de Télédétection des Propriétés Nuageuses (RASTA: Airborne and Ground Radar for Remote Sensing of Cloud Properties; also referred to as Radar System Airborne) airborne cloud radar system.

RASTA, also operated on the Falcon 20, provides zenith and nadir scans of reflectivity at 94 GHz (Protat et al. 2004, 2009). The steps for the treatment of these observations to yield the ice water content are detailed in Fontaine et al. (2014). Table 1 gives a schematic picture of the different steps of this procedure. From analysis of the 2D images of the 2D-S and PIP probes, the number distribution of the hydrometeors $N(D_{max})$ and the distribution of particle aspect ratio $A_s(D_{max})$ were determined as a function of the particle size D_{max}.

In a second step, the reflectivity resulting from the in situ PSD is calculated from the number distribution

and the backscatter coefficients of the hydrometeors. To determine the backscatter coefficient, the **T**-matrix technique of Mishchenko et al. (1996) was applied. This method considers the ice crystals as spheroidal oblates. The axis ratio needed to describe this geometry was taken from the observed particle dimensions D_{max} and H. For the **T**-matrix technique as well as for the following equations, H/D_{max} will be used as aspect ratio A_s of an ice particle.

The refractive index of the ice particles for the wavelength of the cloud radar is also needed. Because the complex shape of crystals is simplified in the **T**-matrix method by an ellipsoid, we assume that its refractive index can be calculated given a mixture of ice and air as in Maxwell Garnett (1904). The crystal mass was supposed to obey the power-law relationship $m = \alpha D_{max}^{\beta}$. Therefore, the ice fraction of each particle and its refractive index also depend on the coefficients α and β. Both were determined by a variational calculation that compares the calculated radar reflectivity at 94 GHz with those measured by RASTA 240 m below and above the airplane. A detailed discussion on the coefficients α and β and the aspect ratio A_s encountered during MT2010 is given in Fontaine et al. (2014).

Using the above given mass–diameter relationship, IWC was calculated using

$$\mathrm{IWC} = \int_{50\,\mu m}^{6.4\,mm} N(D_{max})\alpha D_{max}^{\beta}\, dD_{max}. \tag{1}$$

To apply the result of particle mass to the calculation of the reflectivity of a C-band radar, detailed backscatter calculations as done for 94 GHz were dropped and the Rayleigh approximation was used. Similar to the approach of Hogan et al. (2012), the reflectivity factor Z_{in_situ} was determined by assuming that the particles are oblate spheroids, which are oriented under natural conditions with their longest dimension in the horizontal plane. This leads to

$$Z_{in\_situ} = \frac{1}{|K|^2} \int_{50\,\mu m}^{6.4\,mm} N(D_{max}) D_{equi}^6 \left| \frac{n_{ice}^2 - 1}{1 + P_h(n_{ice}^2 - 1)} \right|^2 dD_{max}, \tag{2}$$

where $|K|^2$ is the dielectric factor and n_{ice} is the complex refractive index of ice. Waves emitted by the MIT C-band radar are polarized horizontally (Williams et al. 1989). The LTHE X-band radar emits horizontally and vertically polarized waves, but we restrict our analysis to only the horizontal component. The geometrical conditions of oblate spheroids are, therefore, expressed by the factor P_h, which depends on the particle's eccentricity e (Doviak and Zrnic 1993; van de Hulst 1957):

$$P_h = \frac{1}{2e} \left[1 - \left(\frac{1 - e^2}{e^2} \right)^{1/2} \arcsin(e) \right] - \frac{1}{2}, \quad \text{with}$$

$$e = [1 - A_s(D_{max})]^{1/2}$$

The eccentricity e is a function of the spheroid's axis ratio for which we used the observed size-dependent aspect ratio A_s.

Instead of expressing the particle volume by D_{max} and A_s [as proposed in Hogan et al. (2012)] the equivalent particle diameter D_{equi} was applied in Eq. (2). The D_{equi} is calculated by

$$D_{equi} = \min\left[D_{max}, \left(\frac{6\alpha}{\pi \rho_{ice}} D_{max}^{\beta} \right)^{1/3} \right], \tag{3}$$

with $\rho_{ice} = 0.917\,\mathrm{g\,cm^{-3}}$. Using $D_{max}^6 A_s^2$ instead of D_{equi}^6 in Eq. (2) yielded unrealistically large reflectivities.

3. Collocation of aircraft and ground radar observations

a. Ground radar observations

The MIT Doppler C-band radar (Russell et al. 2010; Chong 2010) was operated from the Niamey airport, and the polarized Doppler X-band radar (Xport) of LTHE/IRD (Gosset et al. 2010; Koffi et al. 2014) was located 30 km to the southeast of Niamey (for positions see Fig. 1). Both radars are using volumetric scanning protocols, which give a 3D spatial distribution of the reflectivity every 10 min for MIT and every 12 min for the Xport radar. For these volumetric datasets the measurements of MIT and Xport radar cover a horizontal range of 150 and 135 km, respectively. Further specifications for both radars are given in Table 2.

Figure 1 shows radar observations made on 13 August 2010 around 1511 UTC. Both radars give a very similar horizontal structure for the cloud and precipitation fields. From Fig. 1a we can see, though, that the Xport radar detects reflectivity only in a range up to 85 km. Because of the dense cloud field surrounding the Xport in a range of 60–80 km, reflectivities coming from clouds at distances larger 80 km were significantly attenuated.

Figure 2 illustrates the volumetric protocols of both radars. The entire 3D scan takes about 8 min for the MIT radar and almost 12 min for the Xport. The repetition of the scans starts for the MIT every 10 min and for the Xport after 12 min. During the remaining 2 min for the MIT radar, a long-range PPI scan of 250 km and a highly resolved RHI were performed.

Because the aircraft position very often exceeds a distance of 100 km from the radar locations, we will
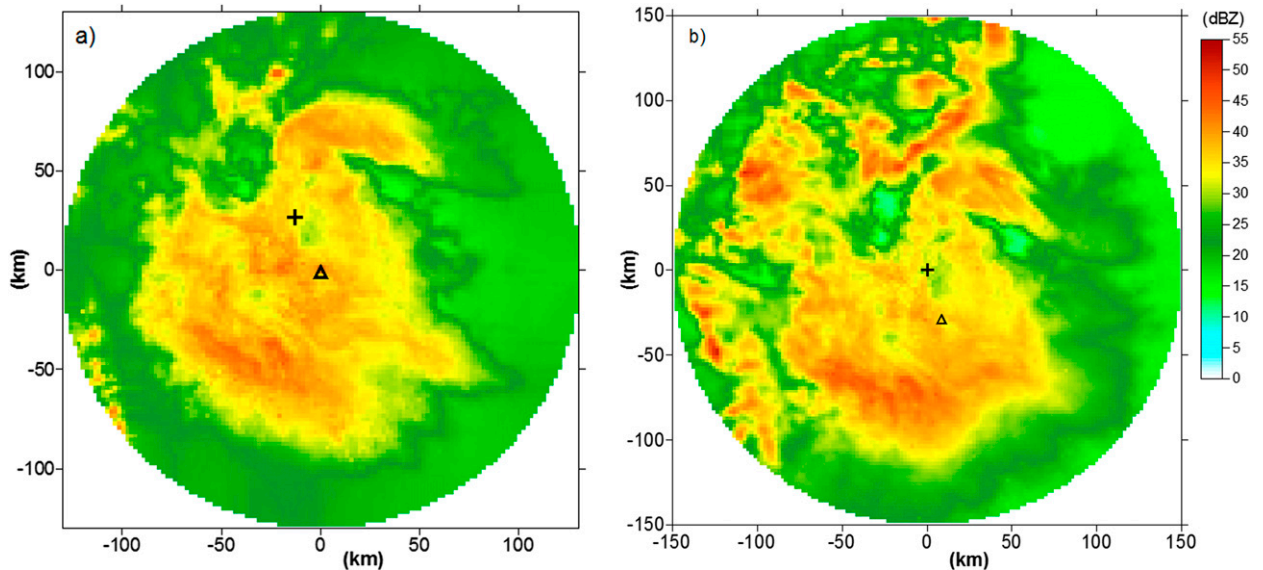
FIG. 1. (a) LTHE/IRD Xport radar at 1511 at elevation 2.62° and (b) MIT C-band observation at 1511 UTC at elevation 2.88°; the plus sign and triangle indicate the locations of the C-band and X-band radars, respectively.

restrict the comparison of aircraft measurements with the radar reflectivity to the MIT C-band observations only.

The presence of the second precipitation radar, however, was useful because it allowed us to validate the reflectivity measurements of the MIT C-band radar. Both radars are attenuated by intense precipitation. On the one hand, the attenuation is stronger for the X-band radar, but, on the other hand, the X-band radar is polarimetric, which allows an attenuation correction on the basis of the differential phase shift (Koffi et al. 2014). Another advantage of polarimetric radar is to monitor the calibration by checking the consistency between the reflectivity and the differential phase shift, the latter being immune to any calibration problem (Testud et al. 2000). In addition, observations with the Xport radar have been successfully compared with the TRMM Precipitation Radar for all of the overpasses occurring in 2010. This allows us to have good confidence in the X-band reflectivity distribution (at least within 85 km of the radar) and to use it as a reference for comparison with the MIT C-band observation.

Comparing individual pulse volumes between two radars creates difficulties that are very similar to those appearing when collocating aircraft and ground

radar observation. The main inconvenience consists in the temporal deviation between both observations as two different volumetric protocols were applied. The displacement between both radars of about 30 km also causes difficulties because the pulse volumes increase with increasing distance from the radar antenna. To collocate the pulse volumes of the Xport radar with those of the MIT radar observations, temporal and spatial interpolation had to be applied for the MIT C-band measurement. The technique used is identical to the one for the aircraft–radar colocalization, which will be presented in the following section 4b.

All Xport pulses inside an 80-km range were compared with the corresponding interpolated values of the MIT radar. Depending on the density of the cloud fields, from 10^6 to 10^7 collocated data points could be compared for an observational period of 2.5 h. Figure 2b shows the frequency distribution of the difference in the observed harmonized reflectivity factors $\Delta Z_{obs} = Z_{Xport} - Z_{MIT}$ between both radars for 13 August 2010. We compared 3.5 million data points for this observational event. The standard deviation of this distribution is about 3.5 dBZ, and further analysis showed that 48% of the compared data couples have deviations of smaller

TABLE 2. Characteristics of the ground radars.

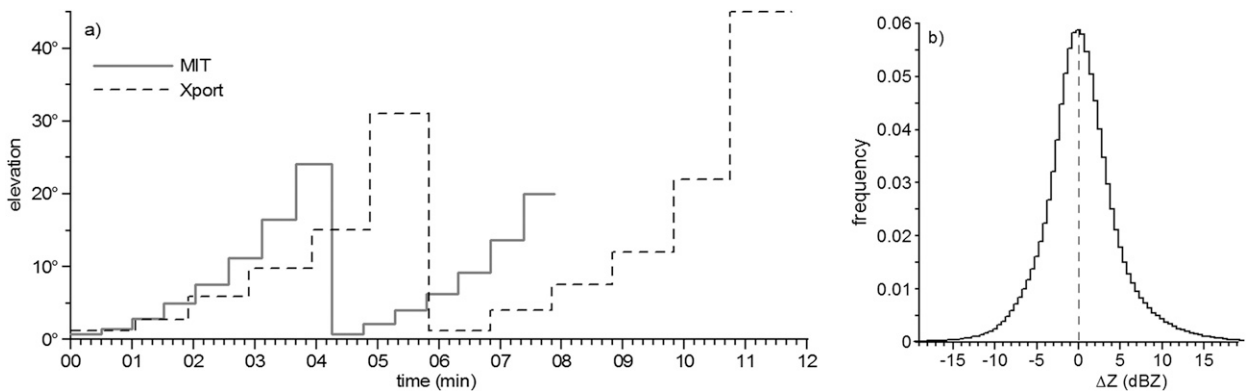|	Frequency	Range	Resolution	Beamwidth	No. of PPI scans
MIT	5.5 GHz	150 km	250 m	1.4°	15 during 8 min
Xport	9.4 GHz	135 km	200 m	1.3°	12 during 12 min

FIG. 2. (a) PPI elevations of the MIT and Xport radars during one volumetric scan. (b) Normalized frequency distribution for ΔZ_{obs} for 13 Aug 2010 (1300–1600); ΔZ_{obs} is the difference between the reflectivity factors ($Z_{Xport} - Z_{MIT}$) after collocating C- and X-band observations.

than $2\,dBZ$, 80% have deviations of smaller than $5\,dBZ$, and 96% have deviations of smaller than $10\,dBZ$.

b. Collocating aircraft and ground radar measurements

As already presented in Fig. 2, radar observations were performed by a regular and uniform protocol, and no specific scanning strategies or specific flight patterns were pursued during MT2010 to match aircraft position and radar sampling volume as, for example, were done by Plank et al. (1980), HEYM05, or HOG06. Consequently, for the analysis of five MT2010 flights, only a very few events occurred for which aircraft and radar sampled the same cloud volume at the same moment (detectable by so-called skin pads on the radar images).

To not restrict our comparison to these very few observational points but to include all available in situ cloud measurements that were in the range of the radar, a spatial and temporal interpolation technique was applied to collocate the aircraft position with the radar pulse volume. Plummer et al. (2010) followed a similar strategy to compare cloud in situ observations with dual-polarization radar measurements collected during the MAP 1999 campaign. To increase the number of aircraft–radar matches, the aircraft-observed wind speed was used to calculate the trajectories of the cloud particles forward and backward of the aircraft over a 300-s period. The reflectivity of the nearest radar pulse volume along this trajectory was taken for comparison with the aircraft in situ observation, as long as vertical and horizontal differences remained smaller than 250 and 1000 m, respectively.

Our method for collocating aircraft position and radar pulse volumes in space is almost identical to the procedure described in detail in Plummer et al. (2010). The aircraft position given by the GPS coordinates

(longitude, latitude, and elevation) is transformed in the spherical coordinate system of the ground radar (range r, azimuth θ, and elevation φ), which can easily be transformed in Cartesian coordinates with the radar location as origin. Because of the high precision of the GPS data, errors in the location of the aircraft resulting from these geometrical calculations are negligible. Because all flights took place in the area from 10° to 14°N, which is very close to the equator, the Earth radius was set to 6376 km.

After locating the aircraft position in the radar's spherical coordinate system, eight radar pulse volumes or reflectivity factors Z surrounding the aircraft can easily be identified, as illustrated in Fig. 3a. To interpolate spatially from the eight neighboring reflectivity signals to the one prevailing at the aircraft position, a so-called interpolation *by inverse distance* is applied. The algorithm for this interpolation of the effective reflectivity Z ($mm^6\,m^3$) at the aircraft position is given by

$$Z(r) = \sum_{i=1}^{8}(w_i Z_i) \Big/ \sum_{i=1}^{8} w_i, \quad \text{with} \quad w_i = (r - r_i)^{-1},$$

where $r - r_i$ are the distances between the aircraft located at r and the eight neighboring measurements of Z_i located at r_i. It becomes evident from Fig. 3a that the distances between aircraft and the center of the surrounding radar voxels depend strongly on the range and elevation of the scanned volume. The role of range and elevation on the size of the radar pulse volume is illustrated in Fig. 3b. Because of the beam divergence, the pulse volume increases significantly with distance from the radar. For elevations up to 9°, scans are very dense and cover all atmospheric layers. For higher elevations, gaps occur between the radar scans, leading to uncertainties
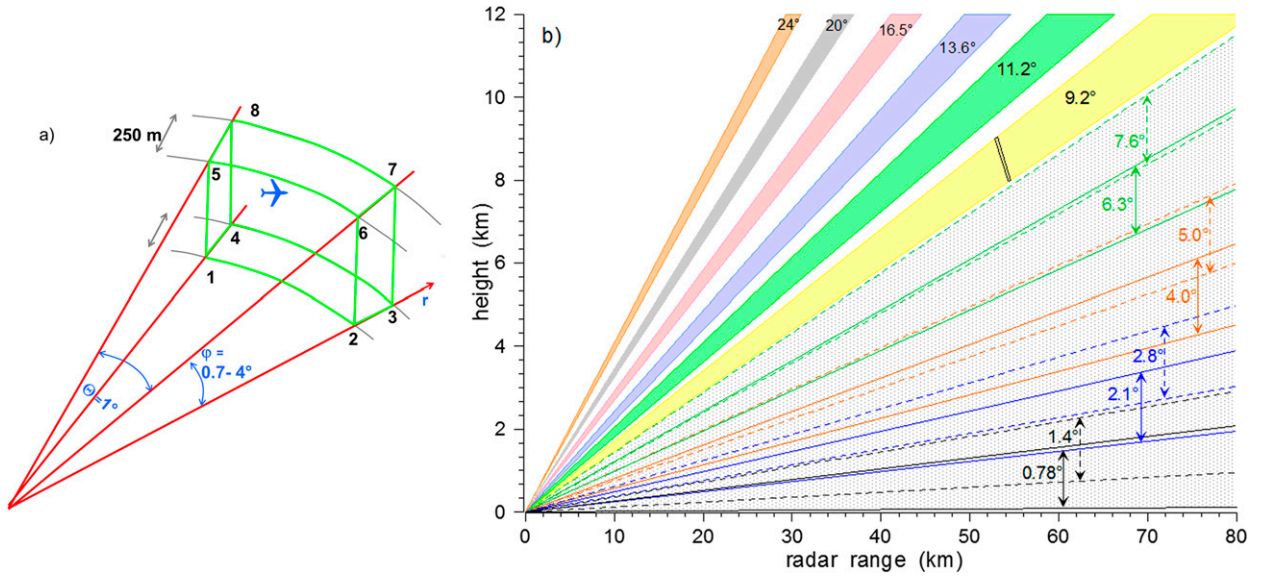
FIG. 3. (a) Aircraft localization in radar coordinates: range r, elevation φ, and azimuth θ. (b) Divergence of the radar beam for the different elevations of the MIT radar. The small black rectangle illustrates the size of a radar pulse volume at 50 km from the radar at 8-km altitude. The ordinate presents the height above 0° elevation.

when interpolating between two successive elevations. This, however, only occurs when distances between aircraft and radar are smaller than 50 km.

For the interpolation in time, a linear approach was used. Because of the radar protocol, each signal $Z(r, \theta, \varphi)$ is observing all locations (r, θ, φ) for every 600 s (every 720 s for the Xport radar). Thus, the reflectivity Z can be calculated for any point in time t within the 10-min period of a volumetric scan using the reflectivity tendencies $\partial_t Z^-$ and $\partial_t Z^+$ for the same radar pulse volume at (r, θ, φ) determined from the previous and following 10-min scans. If the time difference Δt between aircraft and radar for the probing of the same location (r, θ, φ) is negative, the previous tendency $\partial_t Z^-$ is used; otherwise, the tendency of the following 10-min interval $\partial_t Z^+$ is used. The reflectivity can thus be calculated for any time t in a 10-min interval by

$$Z(t_{\text{aircraft}}, r, \theta, \varphi) = Z(t_{\text{radar}}, r, \theta, \varphi)$$
$$+ \partial_t Z^\pm (r, \theta, \varphi) \Delta t, \quad \text{with}$$
$$\Delta t = t_{\text{aircraft}} - t_{\text{radar}}.$$

Because of this linear time interpolation, the time difference between aircraft and radar observation at the same location (r, θ, φ) is always less than 300 s.

The technique to correct the time shift between radar pulse volume and aircraft location by means of aircraft wind measurements as applied by Plummer et al. (2010) or HOG06 was not retained in this study. Cloud layers

investigated during MT2010 still have a very convective character, and therefore wind speed and direction can fluctuate significantly on scales of a few kilometers. In addition, because of the flight strategy during MT2010, aircraft altitude and direction changed frequently (see Figs. 4 and 5), leading to fast alternations in the dynamical conditions.

4. Observational results

a. Flight strategies

The comparison of reflectivity factors from measurements of surface radar and values retrieved from in situ observations is performed only for levels above 5.2 km, where single-phase ice clouds prevailed. This is due to the applied retrieval technique (Fontaine et al. 2014), which actually is restricted to ice crystals only as already presented in Table 1.

Flights took place almost exclusively in the so-called stratiform parts of active squall lines or in deep cloud layers remaining after the disintegration of the system. Figures 4a and 4b give examples of flight patterns and reflectivity structures encountered for flight 18 and flight 15, respectively. For flight 18 on 17 August, a cross-sectional constant-altitude plan position indicator scan (CAPPI) at 9 km was calculated from the 14 PPI scans for the period from 1350 to 1358. The leading front of the squall line extended from the southeast to the northwest for more than 200 km. The continuous line structure of
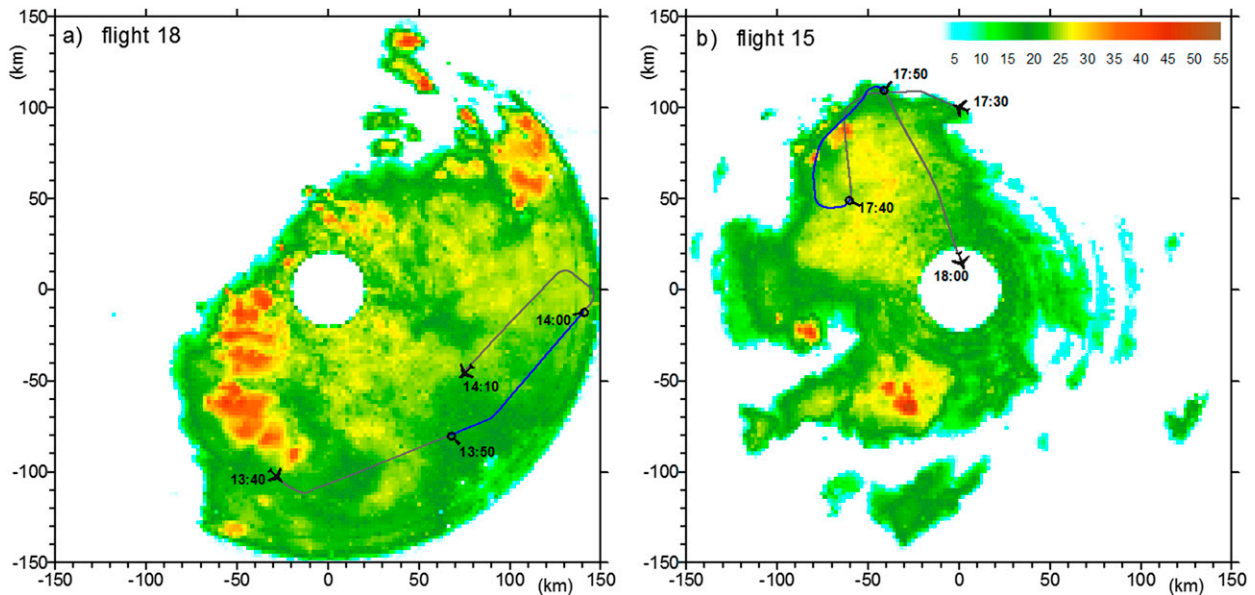
FIG. 4. CAPPI of MIT reflectivity for (a) 1350–1358 UTC during flight 18, at 9-km altitude, and (b) 1750–1758 during flight 15, at 10 km. The blue lines give the aircraft trajectories during these periods; the gray lines give the trajectories 10 min before and 10 min after.

the convective cells encountered during flight 18 became more prominent for altitudes below 5 km (not presented). Figure 4a only depicts those cells shooting to the higher levels for the selected time period. The aircraft stayed at a constant flight level of 9.4 km between 1340 and 1410. We can see from this figure that most cloud fields measured in situ were typically in the range of 15–30 dBZ. In these upper flight levels, higher reflectivities from 35 up to 40 dBZ were only encountered when new cells shot up and thus appeared unexpectedly for the pilot. Figure 4b gives such an example during flight 15 on 6 August, which took place in the debris of the stratiform part of a convective system. Two small convective cells unexpectedly formed between 1730 and 1745 in the north (at $y = 80$ km) at 10-km altitude.

High reflectivity above 40 dBZ also occurred when the aircraft descended to regions of precipitation below the melting level. These situations are best illustrated for flight 18 in Fig. 5a for 1435–1447. As already mentioned, however, this study is restricted to glaciated clouds only.

b. Comparative results

In Figs. 5a–e, the radar reflectivity observed by the MIT radar located on the Niamey airport are compared with the reflectivity calculated from the in situ microphysical observations on board the Falcon 20 aircraft. The collocation technique between aircraft and MIT radar observation was explained in section 3, and retrieval of the ice water content and reflectivity from the airborne measurements was detailed in section 2.

Results illustrated in Figs. 5a–e are taken from five different flights performed during the MT2010 campaign. The results presented here are restricted to the periods in which all airborne instruments (SPEC 2D-S, DMT PIP, and RASTA) were functioning. Depending on the observational day, the analyzed flight periods differ in duration from 40 min for flight 17 up to 2.5 h for flight 18. Figures 5a–e also give the distance of the aircraft from the MIT surface radar (blue lines) and its GPS altitude (green lines). All data presented for both reflectivities in Figs. 5a–e are mean values integrated over 5-s intervals.

In general, we note that in all cases the tendencies of both signals behave very similarly and that their difference remains, for most flights, below a few reflectivity decibels (dBZ). An exception appears for flight 19 (Fig. 5b), for which the calculated in situ reflectivity factor permanently underestimates the observations of the surface radar. This case will be discussed below in more detail.

Despite the averaging over 5-s intervals, both curves show, for all flights, strong short-term variability. The amplitude of these short-term fluctuations is even more pronounced when the cloud fields were patchier, as illustrated in the cases of flight 15 and flight 17. In Fig. 5d one can detect this patchiness of the cloud field by the numerous gaps in the curves for calculated and observed reflectivity (see, e.g., at 1730, 1750, and 1810 in Fig. 5d).

Gaps in the calculated (in situ) reflectivities occur when the retrieval technique for the ice water mass failed. This is obvious for the period from 1435 to 1447 (Fig. 5a) during which the aircraft flew in and below the melting level and the signal of the airborne cloud radar
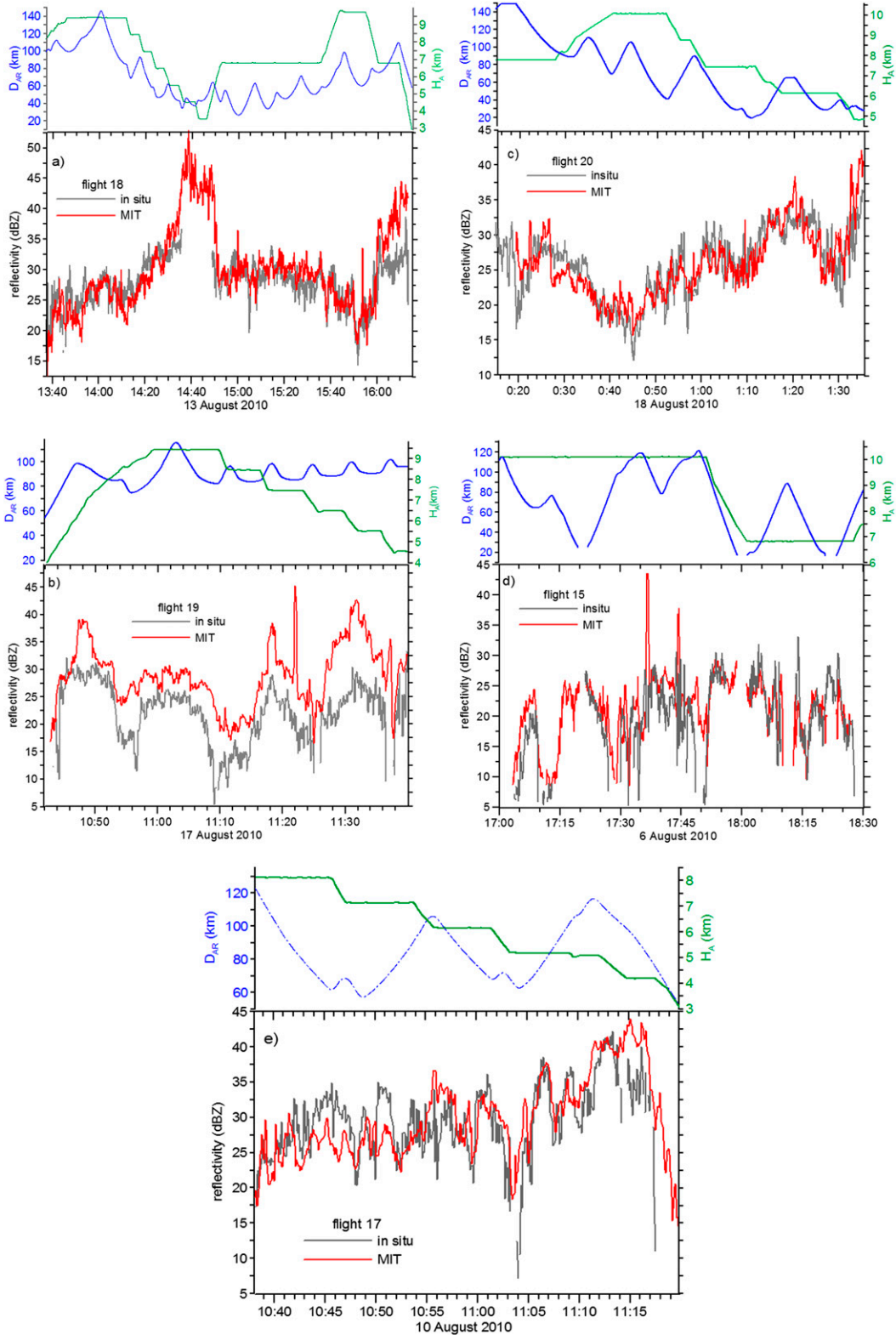
FIG. 5. (a)–(e) Reflectivity factor retrieved from in situ microphysical measurements (gray curve) and reflectivity factor determined from the MIT radar (red curve) by collocating surface observation with the aircraft position. The thin green line represents the aircraft altitude H_A, and the blue line shows the distance D_{AR} between the aircraft and MIT radar at the Niamey airport.

was saturated and thus not exploitable. In elevated layers, unexpected perturbations in the cloud structure can also occur and cause a malfunctioning of the retrieval technique of IWC. This happened, for example, during flight 15 at 1737 and 1744 (Fig. 5d) at which times small convective cells were encountered unexpectedly, as well as during flight 17 for which several gaps appear for the calculated in situ reflectivity (Fig. 5e).

For flight 18, in the time period from 1442 to 1447 the aircraft flew at a constant altitude of 3.5 km—well below the melting layer where temperatures exceeded 3°C. As the optical probes demonstrated that no more ice was present at this level, we calculated the Rayleigh reflectivity from the observed droplet spectra. For the in situ observation, the calculated 5-min mean value of Z resulted in 41.2 dBZ, with a standard deviation of ± 3.0 dBZ. The observed reflectivity from the MIT radar (see Fig. 5a) gives an average value of 43.3 dBZ (± 1.4 dBZ), which deviates little from the calculated value. This result confirms the functioning of our retrieval technique by collocating aircraft and radar voxel in lower altitudes for warm precipitating clouds.

For ice clouds, the most pronounced differences, on the order of 5–10 dBZ, between calculated and observed reflectivity persisting for a couple of minutes can be detected for flight 18 (Fig. 5a) from 1605 to 1612, flight 20 (Fig. 5c) from 0027 to 0035, and flight 17 (Fig. 5e) from 1043 to 1052. Two major reasons can be proposed for these discrepancies. One is the technique for collocation of aircraft and radar sampling volume in time and in space. As already shown in section 3b, significant deviations in time and in altitude can occur between aircraft and radar pulse. From Fig. 3b we can detect that the vertical displacement between two adjacent radar elevations amounts to 2 km at a distance of 50 km between aircraft and ground radar. According to the radar protocol presented in Fig. 2a, it also becomes evident that for the spatial interpolation between the pulse volumes 1–5 and those of the adjacent elevation 9–13, a time shift of ± 4 min has to be taken into account. It is thus possible that the aircraft investigated microphysical properties of cloudy zones, which were, because of the spatial and temporal displacement, different from the values given by the radar pulse volume. A statistical analysis of the horizontal, vertical, and temporal gradients of reflectivity data observed by the MIT radar showed that changes in Z between two successive elevations are typically on the order of ± 3 dBZ. The same order of magnitude was found for temporal variations when comparing Z at the same location but for two consecutive moments. Because of the high resolution in the radial and azimuth directions, horizontal gradients in Z are less than ± 1 dBZ.
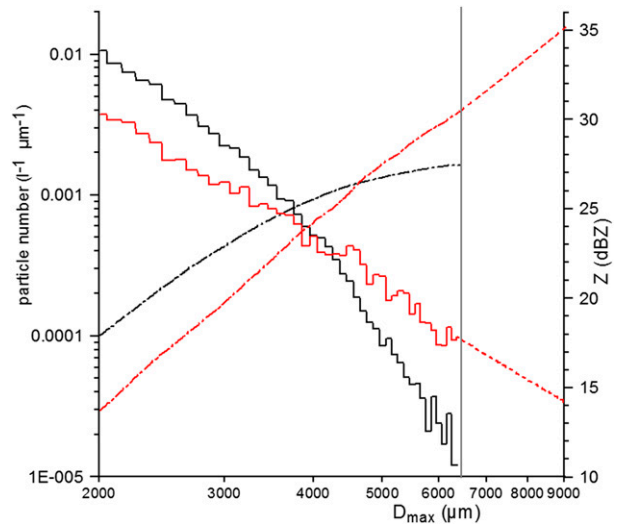

FIG. 6. Number distribution of precipitation sizes for flight 19 observed with PIP. Spectra averaged for 1 min are presented for 1102 (black) and for 1132 (red). The corresponding dash–dotted line depicts the reflectivity increasing with particle size. The upper thin dashed line gives the increase of the reflectivity extrapolating the particle spectrum from 6.4- to 9-mm size.

In this context we also have to emphasize the differences between the sampling volumes of in situ probes and radar pulses. During a 5-s time interval, the optical array probe PIP samples a volume of 1.4 m^3, supposing a constant aircraft speed of 170 m s^{-1}. In contrast to that, the radar pulse volume is much larger. At a distance of 80 km, the radar pulse volume takes 0.75 km^3; at a distance of 150 km, it takes 2.6 km^3.

The second explanation for the discrepancies between in situ and MIT data to persist for several minutes could be the retrieval method for the IWC. The technique developed by Fontaine et al. (2014) actually only allows for the presence of ice particles, with mixed-phase conditions being excluded. Next to the measurements with the airborne microphysical probes and the 94-GHz cloud radar, several hypotheses on particle habits, ice composition, and scattering properties must be made that do strongly affect the resulting cloud water content or its reflectivity as demonstrated in Fontaine et al. (2014).

A critical point for the Z calculation from airborne observations is their limited detection of large precipitating ice crystals. The PIP is restricted to particles sizes below 6.4 mm. The reflectivity at 94 GHz observed by the airborne RASTA is mainly determined by particle sizes smaller than 2 mm, as will be demonstrated later in section 5. For precipitation radars, however, large snowflake-like crystals in the range from some millimeters to exceeding a centimeter are very important.

The role of such large particles on reflectivity is demonstrated in Fig. 6, in which two mean particle
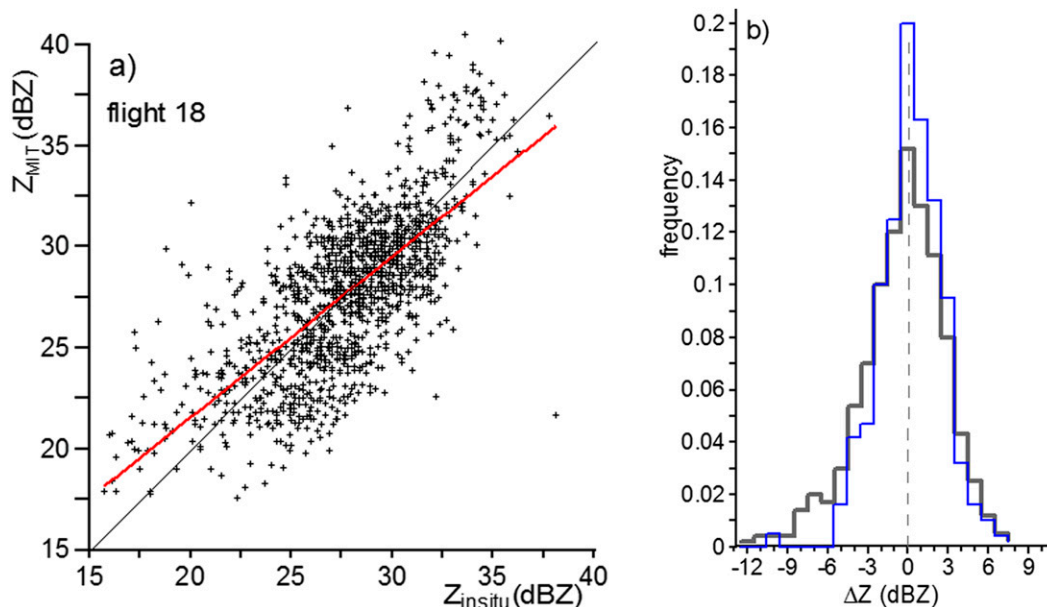
FIG. 7. (a) Scatterplot of the correlation between Z_{MIT} and Z_{in_situ}. (b) Frequency distributions of deviations ΔZ between in situ retrieved reflectivity Z_{in_situ} and collocated reflectivity Z_{MIT} of the surface radar ($\Delta Z = Z_{in\_situ} - Z_{MIT}$). The black line represents the results when taking all observational data points, and the blue line shows when aircraft and radar voxel are deviating by less than 30 s in time and less than 500 m in the vertical direction.

number distributions chosen from flight 19 are presented and compared. The selected two spectra are averages over 1-min time intervals as observed at 1102–1103 and 1132–1133. During the first 1-min period at 1102, the retrieved in situ reflectivity yields a value of 27.5 dBZ (see Fig. 5b) after integration over all particle sizes up to 6.4 mm; for the second period at 1132, the retrieved reflectivity yields 30 dBZ. The collocated reflectivity factor of the MIT radar deviates by 2.5 dBZ from this retrieved value at 1102 but by a much higher amount at 1132 when 40 dBZ were observed by the MIT radar. The size distributions of both cases differ significantly in number and in slope. The spectrum at 1102 (black solid curve in Fig. 6) has a higher concentration for small precipitation sizes, but it decreases more rapidly with increasing particle diameter than the spectrum at 1132 (red solid curve). The consequences for reflectivity become obvious in the same figure. The accumulated reflectivity (dash–dotted lines) shows the value for Z for a given diameter after summing up all contributions from smaller particles. Because of the higher number concentration at $D_{max} = 2$ mm, the spectrum observed at 1102 yields 18 dBZ, but the one at 1132 only yields 14 dBZ. With increasing size, the first particle spectrum decreases rapidly and the accumulated reflectivity converges toward 27.5 dBZ. A convergence for the second spectrum, however, is not visible. Because of a more moderate decline in the number concentration

with increasing particle size, the impact of the larger sizes (>4 mm) on reflectivity remains important. Up to 6.4 mm, no decline in the reflectivity increase appears. We extrapolated this second spectrum observed at 1132 up to 9 mm in D_{max} using the slope of the PSD prevailing in the range from 4 to 6.4 mm (see lower dashed red curve in Fig. 6). As a consequence, reflectivity increases from 30 to 35 dBZ (approaching the observed MIT values). Supposing that in the investigated clouds ice crystals with maximum extensions of more than 1 cm (snowflake-type crystals) were also present, it becomes obvious that an underestimation can occur when the PIP probe and cloud radar observations are employed to determine the reflectivity of a precipitation radar.

For flight 19 (Fig. 5b), the calculated reflectivity factor remains most of the time several reflectivity decibels below the collocated reflectivity of the MIT radar, we can speculate that for this case clouds were charged with large precipitating ice particles. An additional analysis of the PIP images was pursued in which the events for which particle size exceeded the 6.4-mm limit were counted. This analysis (of qualitative character) confirmed that this microphysical behavior prevailed only during flight 19 and at the end of flight 18.

To better quantify the differences between airborne in situ reflectivity and collocated radar reflectivity, some simple statistics were performed. Figure 7a shows the scatterplot of in situ reflectivity Z_{in_situ} versus the

reflectivity of the MIT radar Z_{MIT}. This illustration presents 1340 data points (each averaged over 5 s) of reflectivity measurements for the observations of flight 18. Measurements made in flight levels below 5300 m were excluded from the plot. The bisecting line demonstrates the strong individual scatter between $Z_{\text{in\_situ}}$ and Z_{MIT}. The standard deviation of ΔZ ($=Z_{\text{in\_situ}} - Z_{\text{MIT}}$) yields 2.8 dB$Z$. The red line presents a linear regression. Its regression coefficient is 0.72, and its slope indicates that the retrieved reflectivity below 20 dBZ is mostly underestimated.

Figure 7b (black line) gives the frequency distribution of the deviation ΔZ for observations of all flights, that is, 3450 data points as presented in Fig. 5 (with the exception of flight 19). We can see that the standard deviation is close to 3 dBZ. In addition, it becomes evident that important differences between retrieved and observed reflectivity only occur for the negative branch of the frequency distribution. This means that deviations $\Delta Z > |6 \, \text{dB}Z|$ only occur as a result of underestimation of the reflectivity factor that was calculated from the in situ observations. This result confirms the previous finding that ice clouds investigated during MT2010 are probably characterized by the presence of much larger hydrometeors that can exceed the upper size detection limit of the applied in situ probes.

The blue line in Fig. 7b gives the frequency distribution of ΔZ after constraining our dataset to those observations for which aircraft position and radar voxel deviated vertically by less than 500 m and the probing time by less than 30 s. This restriction reduced the dataset by more than 80%, but the bias between $Z_{\text{in\_situ}}$ and Z_{MIT} decreased noticeably.

5. Relationship between ice water mass and calculated Rayleigh reflectivity

A detailed analysis on the relationship between Z and IWC using the same in situ observations of MT2010 is given in Fontaine et al. (2014). Their analysis is restricted to airborne reflectivity measurements, which were performed by RASTA working at 94 GHz. Their results show that the power law IWC $= 0.0981Z^{0.805}$ is representing well the relationship between both observations (see Fig. 14 and Table 8 in Fontaine et al. 2014). Uncertainties in IWC were found to be $\pm26\%$ for ice water contents ranging between 0.01 and 4 g m^{-3}.

Figures 8a–d show scatterplots of the calculated Rayleigh reflectivity $Z_{\text{in\_situ}}$ (mm^6 m^{-3}) versus the observed values of IWC. The $Z_{\text{in\_situ}}$ was calculated by Eqs. (2) and (3) using the in situ PSD, their ellipsoidal form given by A_s, and their mass characteristics given by α and β. IWC was calculated from Eq. (1). Thus both

IWC and Z_{cal} are provided on the basis of the same microphysical input dataset (PSD, α, and β). Figures 8a–d depict all $Z_{\text{in\_situ}}$–IWC couples for flights 15, 17, 18, and 20, each one separated by the colors red, black, and blue in different temperature regimes. Looking at all data points independent of temperature, we can notice a significant scatter prevailing for all cases. Power slopes are 0.26 and 0.43 for flights 15 and 17, respectively, whereas flight 20 only yields a power slope of 0.13, and for flight 18 an increase of IWC with radar reflectivity entirely disappeared. It is obvious that the weak or nonexistent slopes in Figs. 8c and 8d are due to the lack of reflectivity data of less than 30 mm^6 m^{-3} (15 dBZ) for flights 18 and 20. Most data points in flight 18 and 20 are in the range from 100 to 3200 mm^6 m^{-3} (i.e., 20–35 dBZ). Here, the dispersion of IWC in this reflectivity range is substantial: IWC values in the range from 0.1 up to more than 3 g m^{-3} can occur for the same magnitude of reflectivity. This strong scatter in IWC for Z between 100 and 1000 mm^6 m^{-3} (20 and 30 dBZ) is confirmed by the data presented for flights 15 and 17.

Scatterplots in Figs. 8a and 8b for flights 15 and 17 cover a larger reflectivity range down to Z values of a few reflectivity decibels. For these cases, the tendency that the IWC increases with increasing reflectivity becomes apparent. The scatter, however, remains relatively important, and the resulting regression coefficients R are very low ($R^2 < 0.32$). HEYM05 found similar scatter between Z (at 9.6 GHz) and IWC in ice clouds over Florida. Their data covered the reflectivity range from 10 to 23 dBZ, and the resulting power slope yielded 0.39, similar to Fig. 8b. In addition, HEYM05 noted a change in the slope of the IWC–Z relationship for a reflectivity below 10 dBZ and another change below -10 dBZ. HOG06, who investigated different stratiform clouds over southern England, used the entire range of reflectivity (at 3 GHz) from -20 to almost 20 dBZ and found a power slope of 0.6 in the IWC–Z relationship. They attributed the strong scatter of IWC for a fixed Z to the different temperature conditions under which the IWC was encountered and proposed an IWC(Z, T) relationship that indicated an important increase of IWC with decreasing temperature T for a fixed Z value.

Fontaine et al. (2014) also investigated the temperature effect in the IWC–Z relationship for 94 GHz as observed during MT2010. They found that including temperature in the power fit for IWC had a minor effect and reduced the uncertainty for IWC by 2% only. To clarify the role of temperature for the observations at 5.5 GHz, the data in Figs. 8a–d are split into three temperature ranges: from $-5°$ to $-12°$C (red), from $-12°$ to $-20°$C (black), and below $-20°$C (blue). All panels in Fig. 8 show a tendency that high reflectivity dominates in
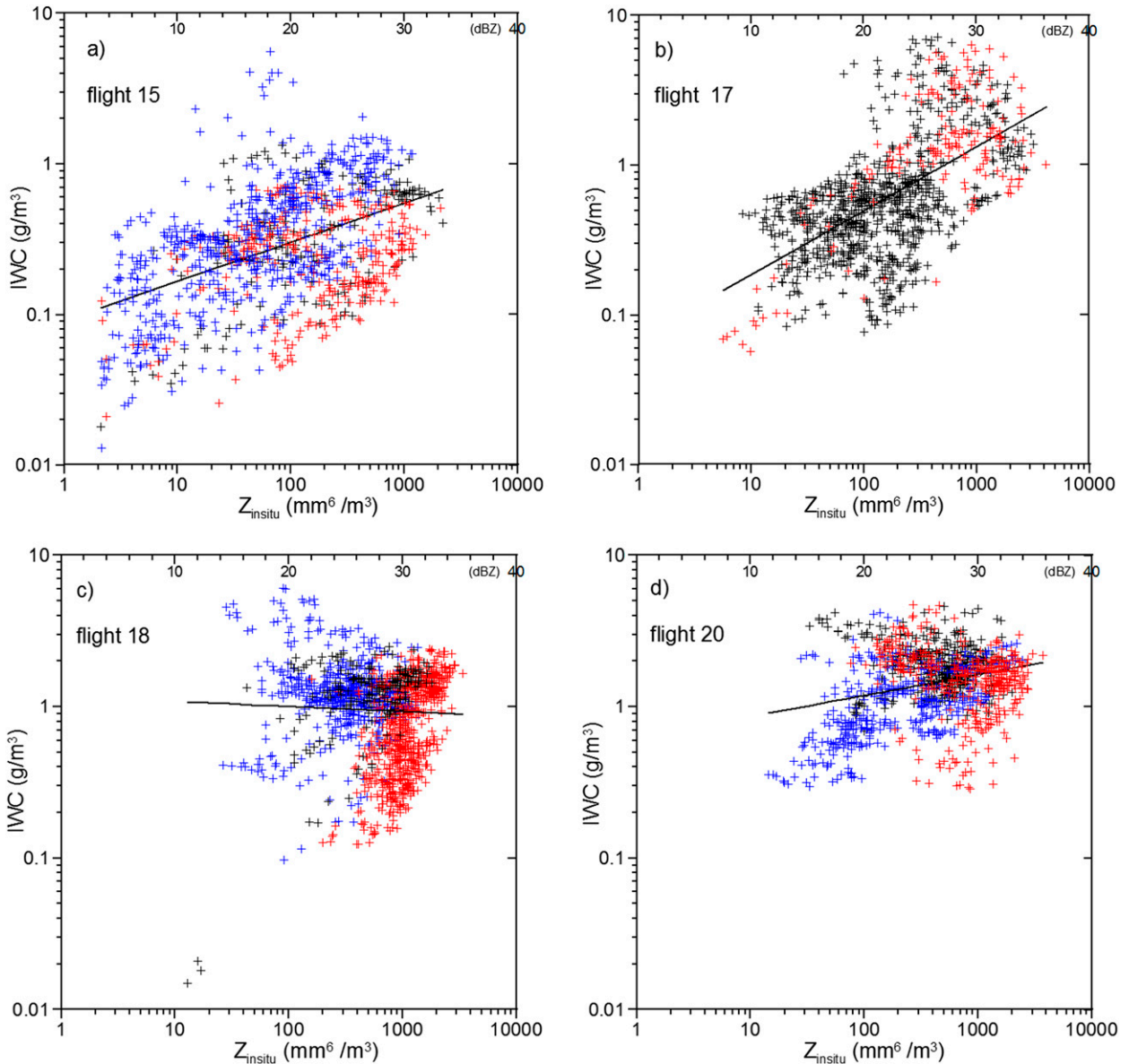
FIG. 8. Scatterplot of radar reflectivity at 5.5 GHz vs ice water content for flights (a) 15, (b) 17, (c) 18, and (d) 20. Red indicates observations from −5° to −12°C, black indicates observations from −12° to −20°C, and blue indicates observations from −20° to −35°C. The upper axes give the corresponding reflectivity factor (dBZ).

the lower cloud layers ($z < 7000$ m) while in the upper layers ($z > 8000$ m) weaker reflectivity prevails. This effect is most pronounced for flight 18 for which most Z measurements larger than 25 dBZ occur in layers from −5° to −12°C while reflectivity for layers from −20° to −33°C are predominantly below 25 dBZ. This separation into high reflectivity for lower cloud layers and low reflectivity for upper cloud layers, however, appears to be less prominent for flights 15, 17, and 20.

According to the approach of HOG06, a temperature decrease from −10° to −25°C causes an IWC increase

from 1 to 2 g m^{-3} for a fixed reflectivity factor of 25 dBZ. Flight 15 (Fig. 8a) supports this behavior to a certain degree. For reflectivity in the range from 20 to 30 dBZ, most data points in the warmer environment have IWC from 0.1 to 0.6 g m^{-3} whereas in the cold temperature regime IWC covers higher values from 0.2 to 1.5 g m^{-3}. For the remaining flights, however, an influence of temperature on IWC is not detectable.

To better understand how dense ice clouds affect the radar reflectivity factor, some individual 1-min-long observations were analyzed in detail with respect to
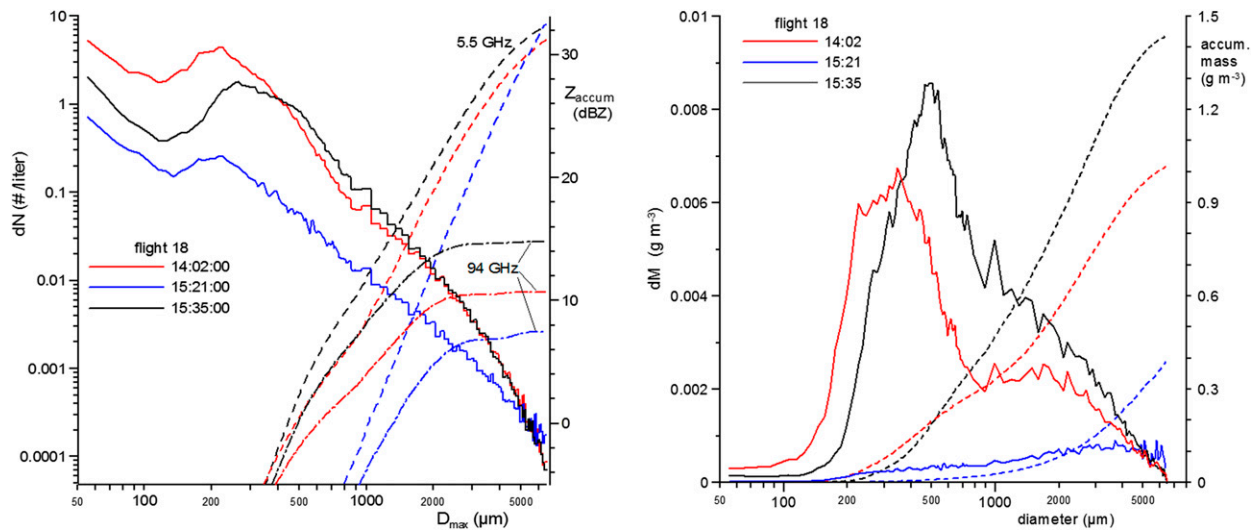
FIG. 9. (left) One-minute-averaged size distributions of ice hydrometeors for three different moments during flight 18 (solid lines). Also shown are accumulated reflectivity values with increasing particle size for radar frequencies of 5.5 (dashed curves) and 94 (dashed–dotted line) GHz. (right) The corresponding mass distributions (solid lines), and the ice mass accumulation with particle size (dashed line).

their microphysical characteristics. The left panel of Fig. 9 depicts three number distributions averaged over 1 min for 1402, 1521, and 1535 UTC as observed during flight 18. During these short periods, all calculated reflectivities range between 31 and 32 dBZ (Fig. 5a) and deviate only slightly from the observations of the MIT radar. The spectra in the period from 1402 to 1403 were measured at an altitude of 9.4 km where $-27°$C prevailed, whereas both other spectra observed after 1500 were collected at 6.8 km at $-10°$C.

The number distributions illustrate that the spectra differ significantly, in particular for small sizes below 200–300 μm. For larger sizes, the spectra for 1402 and 1535 behave somewhat similarly to each other. In contrast to them, the spectrum at 1521 has significantly fewer particles for D_{max} below 4 mm but more particles are present in the range of 5–6.4 mm.

The microphysical differences become more pronounced when illustrating the mass distribution function. The right panel of Fig. 9 depicts the corresponding mass spectra and highlights the differences among the three observations by using a linear axis for $dM(D_{max})$.

It must be pointed out that, following the relationship $m = \alpha(D_{max})^\beta$, calculation of the mass m of ice particles for a fixed size bin D_{max} leads to different results when spectra observed at different times and locations are compared. For each individual spectrum, α and β are retrieved by the technique presented in Fontaine et al. (2014), and thus α and β basically determine the particle mass categorized by its maximum length D_{max}. The effect of time-variable α and β can be detected by comparing mass and number distributions: the intersection

of the curve of the number distribution at 1402 with the one at 1535 occurs in Fig. 9 (left panel) at approximately 400 μm. In contrast to that, the crossing of both mass spectra (Fig. 9; right panel) occurs already at 350 μm. For both observations, the exponent $\beta = 2.24$ was used. The values of α, however, differ, with $\alpha = 0.0067$ at 1402 and $\alpha = 0.0087$ at 1535. The difference in α becomes most prominent for $D_{max} = 500$ μm, at which the mass maximum for the 1535 spectrum occurs and which is 2 times the mass for 500 μm at 1402, whereas the difference in number concentration for 500 μm (Fig. 9; left panel) amounts to only 25% (i.e., 0.2 particles per liter). Measurements at 1535 took place at 6.8 km, whereas those at 1403 were collected at 9.4-km altitude. The retrieved α and β for the observation in the lower level result in a higher crystal density than those retrieved at 9.4 km. Thus at 6.8 km ice particles of all sizes D_{max} exhibit a mass that is superior to that of particles of the same size prevailing at 9.4 km. This result is in agreement with the analysis of the particle images provided by the 2D-S and PIP instruments as well as with conceptual models of cloud-particle evolution in trailing-stratiform regions of mesoscale convective systems (Houze 1993).

Next to the mass spectra (solid lines), the dashed curves in Fig. 9 (right panel) give the mass accumulation with increasing particle size. These curves illustrate well the role of the larger particles for the total ice water content. The major part of the IWC results from particle sizes of greater than 1 mm. The final point of each curve gives the total IWC after integration over the entire spectrum up to 6.4 mm. We can detect important

differences in the total ice content: the spectrum at 1521 contains approximately $0.39\,\mathrm{g\,m^{-3}}$, the one at 1403 contains $1.02\,\mathrm{g\,m^{-3}}$, and the one at 1536 contains $1.44\,\mathrm{g\,m^{-3}}$. This result is certainly surprising, because the reflectivity factor (at 5.5 GHz) of all three cases is very similar.

To understand the contribution of the different particle sizes to the Rayleigh reflectivity we represent the accumulation of reflectivity with increasing particle size in Fig. 9 (left panel). The dashed curves, which relate to the right ordinate, show the accumulated reflectivity Z_{accum} for the precipitation radar (labeled 5.5 GHz) for the three previously discussed observational periods. We can see that all curves end up in the same Z region around 31–32 dBZ. Focusing on the slope of the three curves in the size range of very large particles ($D_{max} > 4$ mm) we note that the reflectivity for cases 1402 and 1535 show a tendency to converge to their final values. For 1521, however, the trend of increasing reflectivity continues beyond the largest particle size (6.4 mm) detectable by the PIP probe. The reason for this behavior is obviously the increased number of particles larger than 5 mm and their slower decrease with size at the trailing end of the spectrum. We can thus conclude from this analysis that the reflectivity as observed by precipitation radars in stratiform and glaciated parts of a deep convective system does not allow us to retrieve reliable (or meaningful) information on the microphysical characteristics and especially on the amount of ice water for the type of clouds investigated over Africa.

This analysis of the influence of ice particle number and size on radar reflectivity was repeated for the frequency of 94-GHz corresponding to the cloud radar employed during MT2010. The dash–dotted curves in the left panel of Fig. 9 illustrate the increase of the accumulated reflectivity for the same particle spectra. We can detect from this that the 94-GHz reflectivity attains its final magnitude in all three cases already for size around 2 mm. Even for the spectrum at 1521, which exhibits high numbers of large particles, only a minor increase in Z_{accum} for sizes from 4 to 6.4 mm is detectable.

The difference in sensitivity to large hydrometeor sizes between radars working typically at low frequencies of 3–10 GHz and cloud radars is caused by their different backscatter properties. Whereas the backscatter coefficient of centimeter-wavelength radar intensifies continuously with the sixth power of particle size, the backscatter of millimeter-wavelength cloud radar does not further increase for sizes above 1–2 mm (Hogan et al. 2012). This distinct behavior suggests that the retrieval of IWC from cloud radar measurements at millimeter wavelengths seems to be more promising

than relying on rain radar observations in the centimeter range.

6. Summary and conclusions

In this study, microphysical observations in deep stratiform layers of ice clouds were compared with reflectivity measurements of a ground-based precipitation radar. The stratiform outflow regions of African squall lines are characterized by high numbers of ice crystals in the range from 0.5 to 2 mm as well as by snowflake-like crystals that occasionally exceed the upper size limit of the in situ instrumentation. The data analyses focused on layers with temperatures between $-5°$ and $-33°$C wherein important IWC and reflectivity factors ranging from 15 and 35 dBZ prevailed. In contrast to other studies in convective cloud (Lawson et al. 2010; Heymsfield et al. 2010) IWC encountered during MT2010 was dominated by precipitation particle sizes of larger than 1 mm.

In situ observations of the size distributions for number, shape, and mass of the hydrometeors (Fontaine et al. 2014) were used to calculate the reflectivity factor using Rayleigh approximation as well as the assumption that particles can be approximated by oblate spheroids. The collocation of this in situ reflectivity with ground radar measurements was attained by a temporal and spatial interpolation of the 4D reflectivity field $Z(t, r, \theta, \varphi)$.

The comparison of the resulting in situ reflectivity factor with the ground C-band measurements showed reasonable agreement in most observational cases. Especially the temporal trends of both coincide very well. The standard deviation between both reflectivity factors in most cases is approximately 3 dBZ. For several periods and especially for flight 19, stronger differences also occurred.

These deviations between calculated in situ reflectivity and ground observation can be attributed to different factors. Errors occurring as a result of the temporal and spatial interpolations must be considered as must a significant size discrepancy between the probing volume of the in situ instruments and the radar pulse volume. From the additional comparison of the MIT C-band with the second surface radar Xport, however, we conclude that the most serious error stems from the time deviation between aircraft and radar occurring when probing the same location. As discussed in section 3a, the intercomparison between MIT and Xport radar was performed using the same interpolation technique as for collocating MIT radar and aircraft (see section 3b). Because the pulse volumes of both radars differ only by a factor of 1.5 and the spatial collocation is also very

accurate, we can suppose that these errors contribute only little to the differences in reflectivity presented in Fig. 2b. The frequency distribution presented in Fig. 2b depicts a shape that is very similar to the ΔZ distribution in Fig. 6b, displaying the deviations between in situ and radar observation. From this we conclude that the time interpolation, which was applied to the ground radar measurements, is probably one of the principal biases in the comparison between in situ reflectivity and ground radar observation. As illustrated in Fig. 7b, moreover, the vertical displacement between aircraft and radar voxels can contribute to the differences in reflectivity.

However, results presented in sections 4 and 5 also indicate that deviations between the calculated in situ reflectivity and radar observations can result when the actual microphysical conditions differ from the hypotheses imposed for calculating the reflectivity factor from the in situ data in accord with Eq. (2). The observed particle spectra show that ice crystal size can well exceed the upper instrumental detection limit and thus cause an underestimation of the calculated reflectivity factors when integrating to 6.4 mm only. Another important uncertainty in the application of Eq. (2) can be attributed to the determination of the particle volume for complex-shaped ice crystals. In this study, the equivalent diameter D_{equi} was used as defined in Eq. (3). The calculation of D_{equi} depends on correct knowledge of the ice mass of the individual particles. Uncertainties in IWC during MT2010 were estimated by Fontaine et al. (2014) to be 24%. For reflectivities ranging from 15 to 35 dBZ, this uncertainty can cause changes of 2–3 dBZ when calculating the reflectivity factor Z. Instead of using D_{equi}, Hogan et al. (2012) used the volume of oblate spheroids given by $(\pi/6)A_s D_{\mathrm{max}}^3$, thus relying on the maximum dimension of the recorded particle size. When this method is applied to the observations of MT2010, all calculated in situ reflectivity factors increase by more than 20 dBZ, thus exceeding by far the observed values from ground radars. We can, therefore, conclude that, for our study, uncertainties in the comparison of ground radar observations with reflectivity factors retrieved from cloud in situ measurements are mainly determined by 1) the temporal differences occurring when probing the same cloudy location and 2) the hypotheses made for the specification of the ice particle volume.

A comparison of the retrieved in situ Rayleigh reflectivity with IWC observed during MT2010 by Fontaine et al. (2014) shows that a linear power-law relationship between IWC and reflectivity factor is only detectable for some flight events. A clear tendency for the IWC to increase with increasing Z becomes evident only when airborne measurements also included thinner cloud regions with reflectivities dropping to 5 or 10 dBZ (see Figs. 8a–d). Most observations in the range from 20 to 30 dBZ illustrate that IWC can yield values from 0.2 to 2 g m^{-3} and more for the same fixed reflectivity factor. A detailed analysis by means of observed size distributions presented in section 5 illustrates that reflectivity factors around 30 dBZ can be caused by very different microphysical conditions. Because large hydrometeors are most important for reflectivity at centimeter wavelengths, the presence of a low number of millimeter-size ice crystals forming weak IWC can result in the same reflectivity as high number concentrations of small ice particles with significantly higher IWC (see Fig. 9).

In contrast to that, millimeter-wavelength cloud radars are almost insensitive to the presence of ice crystals of larger than 2 mm. Consequently, their reflectivity factor correlates much better with the IWC, which is predominantly determined by the particles in the size range from 200 μm to 2 mm. This good functioning of the IWC–$Z_{94\mathrm{GHz}}$ power relationship for the observations made during MT2010 was demonstrated in Fontaine et al. (2014). In summary, we find that a power-law relationship between IWC and reflectivity factor Z of precipitation radars is rarely an appropriate method to gain reliable information on the microphysical properties of dense ice-phase clouds.

REFERENCES

Brandes, E. A., J. Vivekanada, J. D. Tuttle, and C. J. Kissinger, 1995: A study of thunderstorm microphysics with multiparameter radar and aircraft observations. *Mon. Wea. Rev.*, **123**, 3129–3142, doi:10.1175/1520-0493(1995)123<3129:ASOTMW>2.0.CO;2.

Brown, P. R., and P. N. Francis, 1995: Improved measurements of the ice water content in cirrus using a total-water probe. *J. Atmos. Oceanic Technol.*, **12**, 410–414, doi:10.1175/1520-0426(1995)012<0410:IMOTIW>2.0.CO;2.

Chong, M., 2010: The 11 August 2006 squall-line system as observed from MIT Doppler radar during the AMMA SOP. *Quart. J. Roy. Meteor. Soc.*, **136** (S1), 209–226, doi:10.1002/qj.466.

Doviak, R. J., and D. S. Zrnic, 1993: *Doppler Radar and Weather Observations*. 2nd ed. Academic Press, 562 pp.

Field, P. R., R. Wood, P. R. A. Brown, P. H. Kaye, E. Hirst, R. Greenaway, and J. A. Smith, 2003: Ice particle interarrival times

measured with a fast FSSP. *J. Atmos. Oceanic Technol.*, **20**, 249–261, doi:10.1175/1520-0426(2003)020<0249:IPITMW>2.0.CO;2.

——, R. J. Hogan, P. R. A. Brown, A. J. Illingworth, T. W. Choularton, P. H. Kaye, E. Hirst, and R. Greenaway, 2004: Simultaneous radar and aircraft observations of mixed-phase cloud at the 100-m-scale. *Quart. J. Roy. Meteor. Soc.*, **130**, 1877–1904, doi:10.1256/qj.03.102.

——, A. J. Heymsfield, and A. Bansemer, 2006: Shattering and particle interarrival times measured by optical array probes in ice clouds. *J. Atmos. Oceanic Technol.*, **23**, 1357–1371, doi:10.1175/JTECH1922.1.

Fontaine, E., A. Schwarzenboeck, J. Delanoë, W. Wobrock, D. Leroy, R. Dupuy, and A. Protat, 2014: Constraining mass–diameter relations from hydrometeor images and cloud radar reflectivities in tropical continental and oceanic convective anvils. *Atmos. Chem. Phys.*, **14**, 11 367–11 392, doi:10.5194/acp-14-11367-2014.

Gosset, M., E.-P. Zahirb, and S. Moumounic, 2010: Rain drop size distribution variability and impact on X-band polarimetric radar retrieval: Results from the AMMA campaign in Benin. *Quart. J. Roy. Meteor. Soc.*, **136** (S1), 243–256, doi:10.1002/qj.556.

Heymsfield, A. J., and J. L. Parrish, 1978: A computational technique for increasing the effective sampling volume of the PMS two-dimensional particle size spectrometer. *J. Appl. Meteor.*, **17**, 1566–1572, doi:10.1175/1520-0450(1978)017<1566:ACTFIT>2.0.CO;2.

——, Z. Wang, and S. Matrosov, 2005: Improved radar ice water content retrieval algorithms using coincident microphysical and radar measurement. *J. Appl. Meteor.*, **44**, 1391–1412, doi:10.1175/JAM2282.1.

——, C. Schmitt, A. Bansemer, and C. H. Twohy, 2010: Improved representation of ice particle masses based on observations in natural clouds. *J. Atmos. Sci.*, **67**, 3303–3318, doi:10.1175/2010JAS3507.1.

Hogan, R. J., P. N. Francis, H. Flentje, A. J. Illingworth, M. Quante, and J. Pelon, 2003: Characteristics of mixed phase clouds. I: Lidar, radar and aircraft observations from CLARE98. *Quart. J. Roy. Meteor. Soc.*, **129**, 2089–2116, doi:10.1256/rj.01.208.

——, M. P. Mittermaier, and A. J. Illingworth, 2006: The retrieval of ice water content from radar reflectivity factor and temperature and its use in evaluating a mesoscale model. *J. Appl. Meteor.*, **45**, 301–307, doi:10.1175/JAM2340.1.

——, L. Tian, P. R. A. Brown, C. D. Westbrook, A. J. Heymsfield, and J. D. Eastment, 2012: Radar scattering from ice aggregates using the horizontally aligned oblate spheroid approximation. *J. Appl. Meteor.*, **51**, 655–671, doi:10.1175/JAMC-D-11-074.1.

Houze, R. A., 1993: *Cloud Dynamics.* International Geophysics Series, Vol. 53, Academic Press, 573 pp.

Koffi, A. K., M. Gosset, E.-P. Zahiri, A. D. Ochou, M. Kacou, F. Cazenave, and P. Assamoi, 2014: Evaluation of X-band polarimetric radar estimation of rainfall and rain drop size distribution parameters in West Africa. *Atmos. Res.*, **143**, 438–461, doi:10.1016/j.atmosres.2014.03.009.

Korolev, A., and G. A. Isaac, 2005: Shattering during sampling by OAPs and HVPS. Part I: Snow particles. *J. Atmos. Oceanic Technol.*, **22**, 528–542, doi:10.1175/JTECH1720.1.

——, and P. R. Field, 2015: Assessment of the performance of the inter-arrival time algorithm to identify ice shattering artifacts in cloud particle probe measurements. *Atmos. Meas. Tech.*, **8**, 761–777, doi:10.5194/amt-8-761-2015.

Lawson, R. P., and P. Zudema, 2009: Aircraft microphysical and surface based radar observations of summertime Arctic clouds. *J. Atmos. Sci.*, **66**, 3505–3529, doi:10.1175/2009JAS3177.1.

——, E. Jensen, D. L. Mitchell, B. Baker, Q. Mo, and B. Pilson, 2010: Microphysical and radiative properties of tropical clouds investigated in TC4 and NAMMA. *J. Geophys. Res.*, **115**, D00J08, doi:10.1029/2009JD013017.

Matrosov, S. Y., A. V. Korolev, and A. J. Heymsfield, 2002: Profiling cloud ice mass and particle characteristic size from Doppler radar measurements. *J. Atmos. Oceanic Technol.*, **19**, 1003–1018, doi:10.1175/1520-0426(2002)019<1003:PCIMAP>2.0.CO;2.

Maxwell Garnett, J. C., 1904: Colours in metal glasses and metallic films. *Philos. Trans. Roy. Soc. London*, **203**, 385–420, doi:10.1098/rsta.1904.0024.

Mishchenko, M. I., L. D. Travis, and D. W. Mackowski, 1996: **T**-matrix computations of light scattering by nonspherical particles: A review. *J. Quant. Spectrosc. Radiat. Transfer*, **55**, 535–575, doi:10.1016/0022-4073(96)00002-7.

Plank, V. G., R. O. Berthel, and A. A. Barnes Jr., 1980: An improved method for obtaining the water content values of ice hydrometeors from aircraft and radar data. *J. Appl. Meteor.*, **19**, 1293–1299, doi:10.1175/1520-0450(1980)019<1293:AIMFOT>2.0.CO;2.

Plummer, D. M., S. Göke, R. M. Rauber, and L. DiGirolamo, 2010: Discrimination of mixed- versus ice-phase clouds using dual-polarization radar with application to detection of aircraft icing regions. *J. Appl. Meteor.*, **49**, 920–936, doi:10.1175/2009JAMC2267.1.

Protat, A., and Coauthors, 2004: Le projet RALI: Combinaison d'un radar et d'un lidar pour l'étude des nuages faiblement précipitants (The RALI project: The combination of a radar and a lidar to study weakly precipitating clouds). *Meteorologie*, **47**, 23–33.

——, J. Delnoë, P. T. May, D. Bouniol, A. J. Heymsfield, A. Bansemer, and P. Brown, 2007: Evaluation of ice water retrievals from cloud radar reflectivity and temperature using a large airborne in situ microphysical database. *J. Appl. Meteor.*, **46**, 557–572, doi:10.1175/JAM2488.1.

——, ——, A. Plana-Fattori, A. Hasson, E. O'Connor, U. Görsdorf, and A. J. Heymsfield, 2009: Assessment of *CloudSat* reflectivity measurements and ice cloud properties using ground-based and airborne cloud radar observations. *J. Atmos. Oceanic Technol.*, **26**, 1717–1741, doi:10.1175/2009JTECHA1246.1.

Russell, B., and Coauthors, 2010: Radar/rain-gauge comparisons on squall lines in Niamey (Niger) for the AMMA. *Quart. J. Roy. Meteor. Soc.*, **136** (S1), 289–303, doi:10.1002/qj.548.

Testud, J., E. Le Bouar, E. Obligis, and M. Ali-Mehenni, 2000: The rain profiling algorithm applied to polarimetric weather radar. *J. Atmos. Oceanic Technol.*, **17**, 332–356, doi:10.1175/1520-0426(2000)017<0332:TRPAAT>2.0.CO;2.

van de Hulst, H. C., 1957: *Light Scattering by Small Particles.* Courier Dover, 470 pp.

Williams, E. R., S. G. Geotis, and A. B. Bhattacharya, 1989: A radar study of the plasma and geometry of lightning. *J. Atmos. Sci.*, **46**, 1173–1185, doi:10.1175/1520-0469(1989)046<1173:ARSOTP>2.0.CO;2.

Zong, R., L. Liu, and Y. Yin, 2013: Relationship between cloud characteristics and radar reflectivity based on aircraft and cloud radar co-observations. *Adv. Atmos. Sci.*, **30**, 1275–1286, doi:10.1007/s00376-013-2090-7.